Jagannath University Journal of Science
Volume 12, Number I, Jun. 2025, pp. 65−86
https://jnu.ac.bd/journal/portal/archives/science.jsp
ISSN 3005-4486 (Online), ISSN 2224-1698 (Print)

Natural Convective Heat Transfer inside a Square Cavity Filled with Hybrid Nanofluid under the influence of Oblique Variable Magnetic Field with Statistical Analysis

Research Article

Md. Nurul Huda[a*], Mahede-Ul-Hassan[b]
[a]*Department of Mathematics, Jagannath University, Dhaka-1100, Bangladesh*
[b]*Department of Mathematics and Statistics, Bangladesh University of Business and Technology, Dhaka-1216, Bangladesh*

DOI: https://doi.org/10.3329/jnujsci.v12i1.89620

Received: 10.08.2025, Accepted: 25.02.2026, Published: July 2026

ABSTRACT

The optimization and sensitivity analysis of the unsteady natural convective heat transfer flow of Cu-Al_2O_3/H_2O hybrid nanofluid in a square cavity under the influence of an oblique variable magnetic field are investigated numerically and statistically in this work. Brownian motion is taken into account in the hybrid nanofluid thermal conductivity model. The dimensionless governing equations with a sinusoidal boundary condition applied to the left heated wall have been solved using the Galerkin-based finite element method. A substantial degree of agreement is found after a comparison with earlier published findings. Results pertaining to average *Nu* and isotherms are presented. Tabular and graphical forms are used to present the Nu_{ave}. The study analyzes the sensitivity of parameters including λ, d_p and the hybrid nanoparticle volume percentage using response surface methods. The process can be optimized and the best conditions for achieving the highest heat transfer rate can be found by using response surface policy. The magnetic field and its alignment have a major impact on the hybrid nanofluid's flow pattern. The findings show that when the hybrid nanoparticle volume percentage, *Ra* and magnetic field inclination angle increase, the average *Nu* increases significantly. On the other hand, the diameter of the nanoparticles and the Hartmann number have opposing effects. The average *Nu* increases by 48.55% for $Ra = 10^4$ with $\phi_{hnp} = 0.03$ and by 18.53% for the other case when Brownian motion is taken into account.

Keywords: *Hybrid Nanofluid, Periodic Magnetic Field, Response Surface Methodology, Brownian Motion, Finite Element Method*

[*]**Corresponding author**: Md. Nurul Huda
E-mail: mnurulhdu@yahoo.com

1. Introduction

The use of energy by human beings is increasing every day. Enhancing thermal efficiency (TE) and minimizing heat dissipation are crucial in energy conversion systems. Because of the rising necessity for competent heat transfer (HT) fluids in technological and industrial applications, researchers have focused a great deal of attention on nanofluids (NaFs) in various forms of cavities in the presence of magnetic field (MaF) in the last twenty years. One of their main goals has been to increase the HT rate in thermal systems, as HT in conventional fluids has poor thermal conductivity (κ), which limits the ability to enhance the thermal presentation. A variety of different approaches were employed to enhance the HT rate in order to achieve an optimal level of TE. An effective strategy for completing this objective involves the utilization of enrichment in κ. In the beginning, (Maxwell 1873 and Choi 1995) demonstrated the potential for increasing the κ of a mixture of solid and liquid by growing the volume % of nanoparticles (NPs). An experimental investigation was recently conducted on nanofluids using two separate categories of NaPs disseminated in a base fluid (BF). This combination is mentioned to as a hybrid NaF, which is an enhanced version of NaF (Jana et al. 2007, Suresh et al. 2011). This hybrid NaF may possess κ that is greater than that of the basic nanofluids and is capable of handling several applications in typical heat transfer domains.

Since then, detailed evaluations of the original features of hybrid nanofluids have been conducted using either experimental or numerical methods (Maxwell 1873, Choi 1995, Ho et al. 2010, Suresh et al. 2011, Alam et al. 2016). This study concluded that hybrid nanofluid can exhibit more κ behavior compared to BF. The overall finding suggests that the HT rate may be higher for hybrid NaF compared to simple nanofluids and BF. Additionally, the heat HT rate varies depending on the specific model and kind of nanofluids used, taking into account the TpCs of nanofluids. It should be noted that there are no specific TpCs established for decisive the thermophysical properties of hybrid NaFs. (Ben-Cheikh et al. 2013) employed a finite volume approach in conjunction with a multi-grid procedure to conduct a mathematical study on free convection (CnV) in a four-sided vicinity that is non-uniformly heated. The vicinity was occupied with dissimilar NaFs containing various NaPs. The study shows that the HT rate increases as the volume % of NaPs increases for a given Rayleigh number, and this relationship is highly influenced by the nanofluids. Additionally, they discovered the highest heat transfer when utilizing Cu or Ag NaPs, and the lowest when using TiO_2. (Devi and Devi 2017) inspected the flow of a boundary layer of Al_2O_3-Cu/H_2O hybrid NaF over a sheet that is being stretched. Their results indicate an increase of 11.2% in Nu_{ave} compared to the Cu-H_2O nanofluid when a 6% volume fraction of alumina NaPs is added. The thickness of the momentum and temperature boundary layers is greater for Al_2O_3-Cu/water hybrid NaF in comparison to Cu-H_2O NaF. (Sivaraj and Sheremet 2017) conducted a numerical analysis of free CnV in a tending permeable vicinity with a square solid block, considering the impact of MaF orientations. The finite volume approach was employed to solve the governing equations. Their findings demonstrated that the convective HT rate is reduced when the MaF is included, and it also exhibits a non-linear variation of Nu_{ave} as the inclination angle of the MaF increases. In their study, (Yildiz et al. 2019) did a comparative analysis of the HT performance of a hybrid NaF in a square cavity. The aim was to establish theoretical and experimental correlations for the natural CnV process. A proprietary tool utilizing the finite volume approach was employed to calculate the solutions. The results suggest that hybridization can achieve comparable HT enhancement at smaller volume fractions of NaPs for mono-NaFs. It is worth mentioning that the HT rate increases as the values of *Ra* and VF increase. (Rahman et al. 2022) examined the efficiency of free convective HT in a rectotrapezoidal cavity filled with Al_2O_3-Cu/water hybrid NaF. Their findings demonstrated that the thermal buoyancy parameter exerts a momentous inspiration on the configurations of heat lines, isotherms and streamlines. In addition, they compute the thermal allocation coefficient and friction factor. In a recent study by Alam et al. (2023), scrutinized the efficiency of free convective thermal transmission performance of Fe_3O_4-H_2O NaF in a four-sided vicinity filled with aluminum foam permeable medium under the consequence of inclined periodic MaF. Their findings demonstrated that the HT rate and average *Nu* increase significantly for the intensification of NaP volume %, *Ra*, *Da* and period number but opposite trend is found for the *Ha* as well as porosity. It has been found that leaning angle of the periodic MaF has the non-monotonic impact of the HT presentation.

The response surface methodology is beneficial for analyzing phenomena consistently affected by several input sources (Alam et al. 2024) and is employed in HT issues to assess the influence of numerous factors or parameters on the Nusselt number. This procedure facilitates the identification and quantification of the principal components that affect the Nu_{ave}. ReS methodology has been utilized to improve the TE of various HT devices, resulting in more operative cooling and heat exchanger arrangements. This methodology offers a comprehensive framework for evaluating the influence of many essential parameters on system performance (Haque et al. 2024, Keya et al. 2024). The application of response surface approach has improved the TE of numerous HT devices, resulting in the progress of more effective cooling and heat exchanger schemes. The practical inferences of our research in HT and scheme optimization underscore the significance of our discoveries.

Existing research has explored various geometric designs of solar thermal collectors to accommodate different accessible nanofluids with varying TpCs, based on the aforementioned common benefits of hybrid nanofluid-based solar thermal collectors. While extensive study has been conducted on the Cu-Al_2O_3/H_2O hybrid nanofluid, there is still room for improvement in addressing heat loss and enhancing the efficiency of thermal collectors by utilizing hybrid nanofluid in conjunction with appropriate TpCs. The objective of this study is to quantitatively explore the unsteady free convective HT of Cu-Al_2O_3/H_2O hybrid NaF inside a square cavity under the influence of oblique variable MaF. The response surface (ReS) methodology has been used as an optimization system after modelling the HT rate in the present work. The ReS scrutiny adds a supplementary level of innovation to this research. The numerical results we obtained provide valuable information for optimizing design and improving the performance of energy systems, such as solar thermal collectors and electronic equipment cooling.

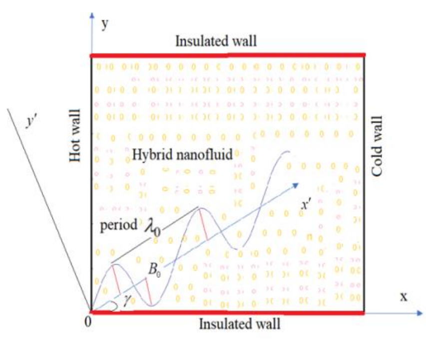

Figure l(a): Physical domain with boundary conditions (BCs).

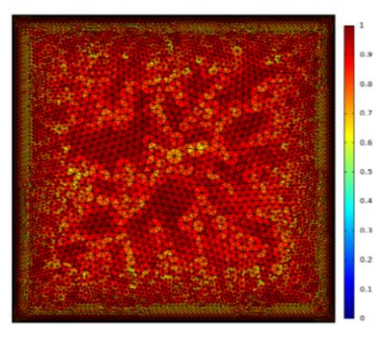

Figure l(b): Mesh generation of the cavity.

2. Physical and mathematical modeling

An unsteady, incompressible, laminar, two-dimensional free convective flow and HT are considered in a square cavity of length *L* as Fig.1(a), filled with Cu-Al_2O_3/H_2O hybrid NaF under the effect of inclined periodic MaF. The inclination angle γ is defined as the angle between the direction of the applied inclined periodic MaF and the positive x-axis in the horizontal plane. The relationship of the inclined periodic MaF is defined as: $B = B_0 \sin[\frac{2\pi}{\lambda_0}(x\cos\gamma + y\sin\gamma)]$, where B_0 and λ_0 represent the amplitude and period of the inclined periodic MaF, respectively. The dimensional coordinates are employed, with the x-axis measuring along the bottom wall and the y-axis being perpendicular to it along the left wall. The left wall of the cavity is heated sinusoidally at a specific temperature $T = T_{c_1} + (T_h - T_{c_1})(\frac{a_0}{L})\sin(\frac{\pi y}{L})$, while the right barrier is cooled at a lower temperature $T = T_{c_1}$. The other two walls of the space are insulated. The gravitational force acts in the negative y-direction, and the effects of Brownian motion (BrM) are accounted for in the flow domain. Thermal equilibrium is also anticipated to be present between the BF and NaPs. All borders are considered to be inflexible and have a no-slip condition.

The examination of engineering systems, including microscale enclosures and electronic cooling units, can greatly benefit from the physical assumptions of unsteady flow, laminar conditions, incompressibility and thermal equilibrium to simplify intricate fluid dynamics. The unsteady assumption is pertinent in situations involving temperature variations and transient heat generation, for as in electrical equipment with fluctuating power outputs. Laminar flow is frequently seen in microscale applications because the small dimensions diminish the impact of inertial forces in comparison to viscous forces, facilitating a streamlined examination of fluid dynamics. The assumption of incompressibility is generally applicable in these systems, especially in low-speed flows where density fluctuations are minimal, permitting the treatment of fluid properties as constant. Finally, the assumption of thermal equilibrium is valid when heat conduction in solid structures and convective processes in the fluid occur rapidly enough to establish a uniform temperature distribution, hence simplifying thermal modeling. Collectively, these assumptions enable a more manageable consideration of thermal management and fluid dynamics in sophisticated engineering systems, guaranteeing efficient design and operation.

Table l: Thermal properties used in this study at room temperature (Rahman et al. 2022).

BF and NaPs	c_p (J/kgK)	ρ (kg/m^3)	κ (W/mK)	$\beta \times 10^{-5}$ $(1/K)$	μ (Ns/m^2)	σ (S/m)	Pr
Al_2O_3	765	3970	40	0.85		35×10^6	
Cu	385	8933	400	1.67		59.6×10^6	
Water	4179	997.1	0.613	21	0.001003	5.5×10^{-6}	6.8377

2.1. Mathematical model

The time-varying 2D hybrid NaF flow can be pronounced by the following governing eqns., which include continuity, momentum and energy eqns. (Belhaj and Ben-Beya 2022):

$$\frac{\partial u}{\partial x} + \frac{\partial v}{\partial y} = 0 \tag{1}$$

$$\frac{\partial u}{\partial t} + u\frac{\partial u}{\partial x} + v\frac{\partial u}{\partial y} = -\frac{1}{\rho_{hnf}}\frac{\partial p}{\partial x} + \frac{\mu_{hnf}}{\rho_{hnf}}\left(\frac{\partial^2 u}{\partial x^2} + \frac{\partial^2 u}{\partial y^2}\right) + \frac{\sigma_{hnf} B_0^2}{\rho_{hnf}}\sin^2[\tfrac{2\pi}{\lambda_0}\left(y\sin\gamma + x\cos\gamma)](v\sin\gamma\cos\gamma - u\sin^2\gamma\right) \tag{2}$$

$$\frac{\partial v}{\partial t}+u\frac{\partial v}{\partial x}+v\frac{\partial v}{\partial y}=-\frac{1}{\rho_{hnf}}\frac{\partial p}{\partial y}+\frac{\mu_{hnf}}{\rho_{hnf}}\left(\frac{\partial^2 v}{\partial x^2}+\frac{\partial^2 v}{\partial y^2}\right)+g\left(T-T_C\right)\frac{(\rho\beta)_{hnf}}{\rho_{hnf}}$$
$$+\frac{\sigma_{hnf}B_0^2}{\rho_{hnf}}\sin^2[\tfrac{2\pi}{\lambda_0}(y\sin\gamma+x\cos\gamma)]\left(u\sin\gamma\cos\gamma-v\cos^2\gamma\right) \tag{3}$$

$$\frac{\partial T}{\partial t}+u\frac{\partial T}{\partial x}+v\frac{\partial T}{\partial y}=\alpha_{hnf}\left(\frac{\partial^2 T}{\partial x^2}+\frac{\partial^2 T}{\partial y^2}\right) \tag{4}$$

2.2. Initial-BCs

The thermal settings are as follows:

For $t=0$, entire domain: $p=0, T=T_{c_1}$ (5a)

For $t>0$,

At the left hot barrier: $T=T_{c_1}+(T_h-T_{c_1})(\frac{a_0}{L})\sin(\frac{\pi y}{L})$, (5b)

At the insulated walls: $\frac{\partial T}{\partial y}=0$ (5c)

At the right cold barrier: $T=T_{c_1}$ (5d)

And $u=0, v=0$: at all walls.

The dimensionless governing eqns. are as follows:

Continuity equation: $\frac{\partial U}{\partial X}+\frac{\partial V}{\partial Y}=0$ (6)

Momentum equations:

$$A\left(\frac{\partial U}{\partial \tau}+U\frac{\partial U}{\partial X}+V\frac{\partial U}{\partial Y}\right)=-\frac{\partial P}{\partial X}+B\Pr\left(\frac{\partial^2 U}{\partial X^2}+\frac{\partial^2 U}{\partial Y^2}\right)$$
$$+E\Pr Ha^2\sin^2[\tfrac{2\pi}{\lambda}(X\cos\gamma+Y\sin\gamma)]\left(V\cos\gamma\sin\gamma-U\sin^2\gamma\right) \tag{7}$$

$$A\left(\frac{\partial V}{\partial \tau}+U\frac{\partial V}{\partial X}+V\frac{\partial V}{\partial Y}\right)=-\frac{\partial P}{\partial Y}+BPr\left(\frac{\partial^2 V}{\partial X^2}+\frac{\partial^2 V}{\partial Y^2}\right)+CRa\Pr\theta$$
$$+E\Pr Ha^2\sin^2[\tfrac{2\pi}{\lambda}(X\cos\gamma+Y\sin\gamma)]\left(U\cos\gamma\sin\gamma-V\cos^2\gamma\right) \tag{8}$$

Energy equation: $$\frac{\partial \theta}{\partial \tau}+U\frac{\partial \theta}{\partial X}+V\frac{\partial \theta}{\partial Y}=D\left(\frac{\partial^2 \theta}{\partial X^2}+\frac{\partial^2 \theta}{\partial Y^2}\right) \tag{9}$$

The above governing eqns. are dimensionless by using the following transformations

$$A_0=\frac{a_0}{L}, X=\frac{x}{L}, Y=\frac{y}{L}, \mathrm{U}=\frac{uL}{\alpha_{bf}}, \mathrm{V}=\frac{vL}{\alpha_{bf}}, \mathrm{P}=\frac{pL^2}{\rho_{bf}\alpha_{bf}^2}, \theta=\frac{T-T_C}{T_h-T_C}, \tau=\frac{t\alpha_{bf}}{L^2}, \upsilon_{bf}=\frac{\mu_{bf}}{\rho_{bf}}, \lambda=\frac{\lambda_0}{L}$$

The corresponding initial and BCs are as follows:

For $\tau=0$, $\theta=0, P=0$ (10a)

For $\tau>0$, the dimensionless BCs:

At hot wall: $\theta=A_0\sin(\pi Y)$ (10b)

At the insulated walls: $\frac{\partial \theta}{\partial Y}=0$ (10c)

At cold wall: $\theta=0$ (10d)

And $U=0, V=0:$ at all walls.

Here, λ is the dimensionless period number, ϒ is the magnetic field inclination angle, τ is the dimensionless time, $A=\frac{\rho_{hnf}}{\rho_{bf}}$, $B=\frac{\mu_{hnf}}{\mu_{bf}}$, $C=\frac{(\rho\beta)_{hnf}}{(\rho\beta)_{bf}}$, $D=\frac{\kappa_{hnf}}{\kappa_{bf}}/\frac{(\rho C_p)_{hnf}}{(\rho C_p)b_{bf}}$, $Ra=\frac{g\,(T_h-T_c)\,\beta_{bf}\,L^3}{\alpha_{bf}\,\upsilon_{bf}}$ (Rayleigh number), $E=\frac{\sigma_{hnf}}{\sigma_{bf}}$, $\Pr=\frac{\upsilon_{bf}}{\alpha_{bf}}$ (Prandtl number), $Ha=B_0 L\sqrt{\frac{\sigma_{bf}}{\mu_{bf}}}$ (Hartmann number), $\phi_{hnp}=\phi_{Al_2O_3}+\phi_{Cu}$, (ϕ_{hnp} is the NaP volume fraction of the hybrid NaF), $\mu_{hnf}=\frac{\mu_{bf}}{\left(1-\phi_{hnp}\right)^{2.5}}$, $\alpha_{hnf}=\frac{\kappa_{hnf}}{(\rho C_p)_{hnf}}$,

$\rho_{hnf}=\rho_a\phi_{Al_2O_3}+\rho_c\phi_{Cu}+(1-\phi_{hnp})\rho_{bf}$, $(\rho C_p)_{hnf}=\phi_{Al_2O_3}(\rho C_p)_a+\phi_c(\rho C_p)_c+(1-\phi_{hnp})(\rho C_p)_{bf}$,

$\sigma_{hnf}=\sigma_{bf}+\frac{3\sigma_{bf}(\sigma_{np}-\sigma_{bf})\phi_{hnp}}{(\sigma_{np}+2\sigma_{bf})-(\sigma_{np}-\sigma_{bf})\phi_{hnp}}$, $(\rho\beta)_{hnf}=(\rho\beta)_a\phi_{Al_2O_3}+(\rho\beta)_c\phi_{Cu}+(\rho\beta)_{bf}(1-\phi_{hnp})$,

$$\kappa_{hnf}=\frac{\frac{\phi_{Al_2O_3}\kappa_a+\phi_{Cu}\kappa_c}{\phi_{hnp}}+2\kappa_{bf}+2(\kappa_a\phi_{Al_2O_3}+\kappa_c\phi_{Cu})-2\phi_{hnp}\kappa_{bf}}{\frac{\kappa_a\phi_{Al_2O_3}+\phi_{Cu}\kappa_c}{\phi_{hnp}}+2\kappa_{bf}-(\kappa_a\phi_{Al_2O_3}+\kappa_c\phi_{Cu})+\kappa_{bf}\phi_{hnp}}\kappa_{bf}+\frac{(\rho C_p)_{np}\phi_{hnp}}{2D_T^l}\sqrt{\frac{2k_B D_T T_{ref}}{3\pi d_p\mu_{hnf}}}$$

where $\sigma_{np}=\frac{\phi_{Al_2O_3}\sigma_a+\sigma_c\phi_{Cu}}{\phi_{hnp}}$, $(\rho C_p)_{np}=\frac{\phi_{Al_2O_3}(\rho C_p)_a+\phi_{Cu}(\rho C_p)_c}{\phi_{hnp}}$

and $D_T=0.126\frac{\kappa_{hnf}\beta_{bf}\mu_{hnf}(0.0002d_p+0.1537)}{\kappa_{bf}\rho_{hnf}}, D_T^l=\sqrt{D_T}$. For κ_{hnf}, the last term on the R.H.S. is due to the BrM of the NaPs. BrM is a consequence of the crashes of the NaPs that are deferred in the base fluid and it is engaged into the TpC correlation.

$Nu_{ave}=\int_0^1 Nu_l\,dY$ where $Nu_l=-\frac{k_{hnf}}{k_{bf}}\left(\frac{\partial\theta}{\partial X}\right)_{X=0}$.

The linked quantities above are exemplary in their nomenclature.

3. Solution schemes

The Galerkin weighted residual finite element method is utilized to solve the governing equations (6) - (9) and the boundary conditions (10a) - (10d). This method discretizes the solution space domain into meshes of finite elements composed of nonuniform triangular elements. The triangular components of the six nodes are utilized to enhance finite element equations that correlate temperature and velocity across all six nodes. All that is associated with the corner nodes is pressure. The governing nonlinear partial differential equations utilize the Galerkin weighted residual method to transform the nonlinear governing equations into a system of integral equations. Utilize Gauss's quadrature method to resolve the integral components of these equations. The nonlinear algebraic equations are subsequently adjusted utilizing BCs. Additionally, the Newton-Raphson method is employed to resolve these nonlinear algebraic equations in matrix representation. The standard convergence conditions for the numerical solution are $|l^{r+1}-l^r|\leq 10^{-5}$, where $l\in\{\theta,U,V\}$ and *r* denotes the number of iterations. Additionally, the ReS methodology is utilized to assess the FEM-generated data with statistical software tools such as Design Expert. The MATLAB software is utilized for graphical representation. The Core i5 laptop is utilized for numerical computations. The details of this approach can be located in the investigation of Zienkiewicz and Taylor (1991) and Alam et al. (2016).

3.1 Mesh generation

Within the framework of the FEM, the task of constructing a mesh entail partitioning a specified domain into a set of reduced sub-domains referred to as finite elements. The numerical grids have been tactically placed at precise points within the domain to estimate the variables of the existing problem. Consequently, it is essentially a distinctive depiction of a geometric area. Mesh generation is a crucial phase in establishing the geometric domain for the finite element method, which is an effective technique for addressing boundary value issues across various engineering disciplines. Figure 1(b) illustrates the finite element mesh employed for the current physical work, along by a legend denoting the quality metric.

Table 2: Grid sensitivity test for $Al_2O_3 - Cu / water$ hybrid nanofluid, when $\phi_{hnp} = 0.01$, $Ha = 5$, $\lambda = 0.25, Ra = 10^5, \gamma = \frac{\pi}{4}$, $d_p = 130nm, \tau = 0.7$.

Number of Elements	1308	2124	3258	14796	55728
Nu_{ave}	5.5087	5.5322	5.5754	5.5989	5.6001

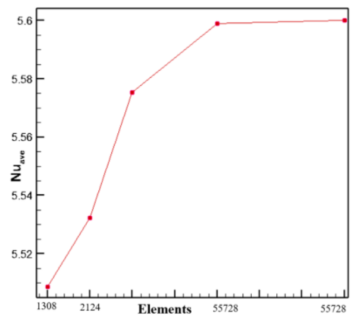

Figure 2: Convergence of Nu_{ave} for varying quantities of elements.

3.2. Grid sensitivity test

In order to determine the appropriate grid size, a grid-independent test is conducted, taking into account $Ha = 5, Ra = 10^5, \gamma = \frac{\pi}{4}, d_p = 130nm,$ $\phi_{hnp} = 0.01,$ $\tau = 0.7, Pr = 6.8377.$ We are now examining five different non-uniform grids with varying numbers of elements within the resolution field: 1308, 2124, 3258, 14796, and 55728. The numerical analysis is conducted to Nu_{ave}gain insight into the grid resolution for the mentioned elements, as presented in Table-2 and Fig.2. The amount of the change in $Nu_{ave}$for 14796 elements is negligible compared to the consequences gained for elements 55728. We have preferred 14796 triangular elements to efficiently address the heat transport of the hybrid nanofluid model and achieve accurate outcomes.

3.3. Code validation

In order to verify the precision of our computed results, we conducted two investigations utilizing the most up-to-date FEM code. The data obtained

(a) $\phi = 0.02$

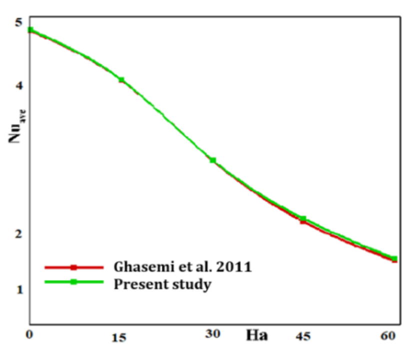

(b)

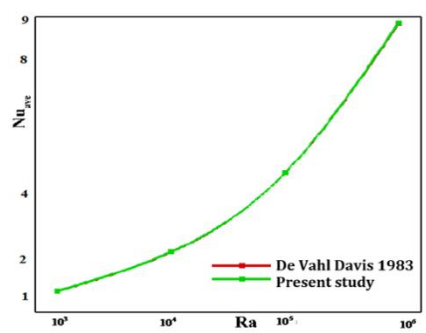

Figure 3: Code validation with existing data (a) Ghasemi et al. (2011) ($\phi = 2\%$) (b) De Vahl Davis (1983) with present study.

from these studies has been documented in published literature. Firstly, we validate our proposed solution process using a Al_2O_3-H_2O nanofluid ($\phi = 0.02$)with Ghasemi et al. (2011). The results obtained under the specified assumptions are presented in Fig. 3(a). The current study and code have been shown to be valid and demonstrate a strong correlation with existing scientific data. Furthermore, the governing equations have been successfully solved for a cavity that is filled with a pure fluid, and the results have been verified using the research conducted by De Vahl Davis (1983). The findings, obtained based on the given assumptions, are displayed in Figure 3(b). It is evident that the current investigation and code are reliable, as they exhibit strong concurrence with the most recent scientific information. Therefore, these findings provide us with confidence that our code can accurately calculate the solution, making it suitable for studying the current situation. Hence, this comparison further confirms the accuracy of our code for future inquiries.

4. Result and discussion

This study examines the effects of the inclined periodic MaF intensity on a square cavity filled with *Cu-Al$_2$O$_3$/H$_2$O* hybrid NaF. The cavity has sinusoidal thermal BC at the heated wall (T_h). The obtained results are described. Calculations are performed for several values of the relevant parameter's inclination angle (γ) of the inclined periodic MaF, including the period (λ), *Ha* and *Ra.* The findings are displayed as isotherms, average Nusselt numbers and a response surface plot derived from the ReS methodology, for varying model parameters. The entire study focuses on the fixed hybrid NaPs VF, with a ratio of 90:10 (Al_2O_3: Cu) NaPs VF in water are tabulated. The primary objective of the outcomes is to determine the exact HT coefficient for a square cavity filled with hybrid NaF for industrial applications.

Fig. 4, shows that at $\tau = 0.1$, the isotherms are positioned next to the heated wall and are in close proximity to each other. As time progresses without any units, the spread of the isotherms occurs from the wall that is being heated to the wall that is cold, and at $\tau = 0.7$ reaching a condition of equilibrium.

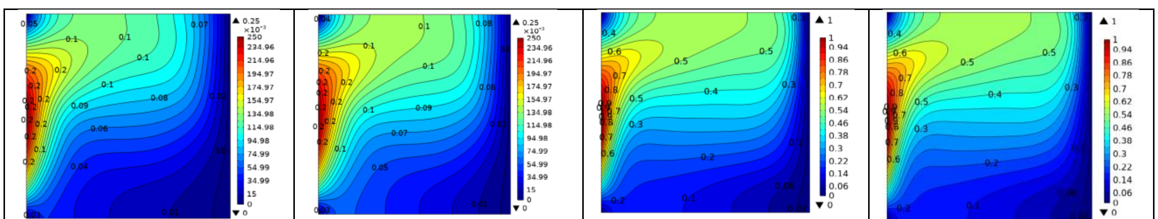

$\tau = 0.1$	$\tau = 0.5$	$\tau = 0.7$	$\tau = 1.7$

Figure 4: Isotherms decoration for dissimilar values of τ when $Ra = 10^5$, $d_p = 130nm$, $\phi_{hnp} = 0.01$, $\gamma = \frac{\pi}{4}$, $\lambda = 0.25$, $Ha = 5$.

The combined effects of *Ha* and *Ra* for $Ha = 5, 45, 100$; $Ra = 10^4, 10^5, 10^6$ on the isotherms are illustrated in Fig. 5. The isotherms are essential in HT with hybrid NaF, since they signify the effective modes of HT and the intensity of CnV. This graphic illustrates that the isotherms are in close proximity T_h to the cavity. The temperature differential at the cavity exceeds that of the cold partition, leading to an elevated HT rate at the cavity surface. As the *Ha* value escalates, the isothermal lines become increasingly compressed, signifying that convection is the predominant mechanism of HT. Furthermore, irrespective of the *Ra* values, the cohesiveness of the isotherm

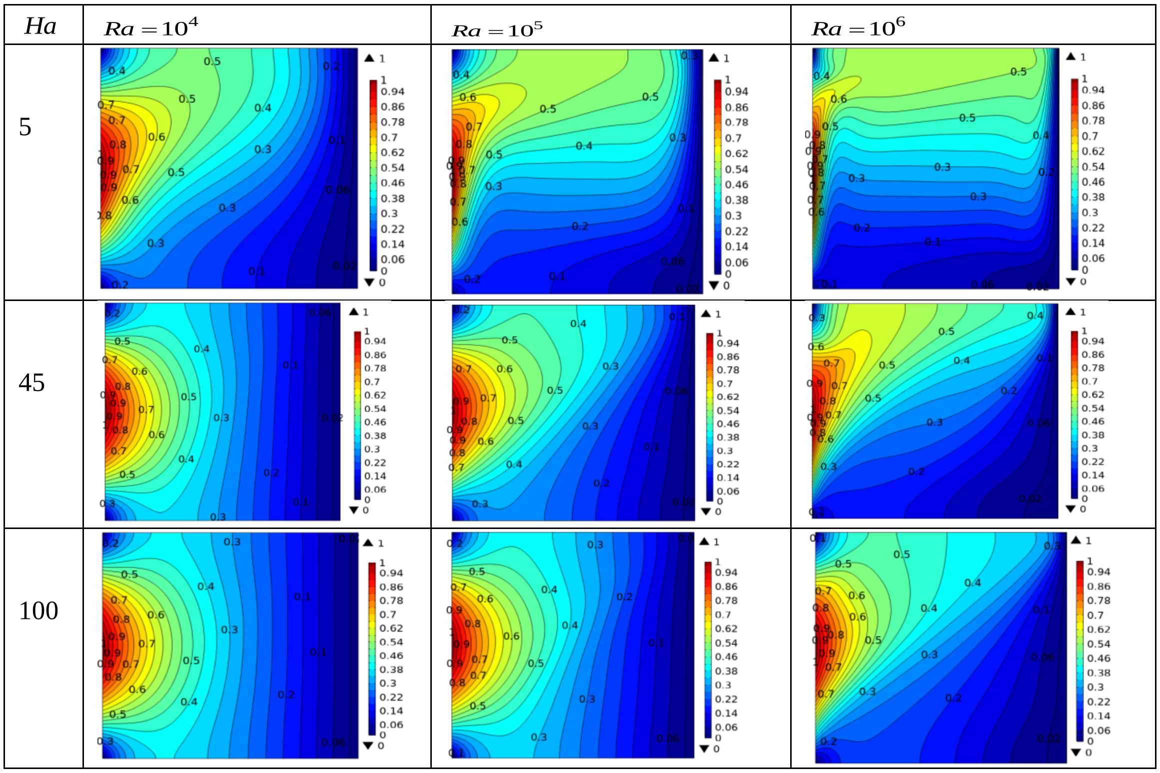

Figure 5: Isotherms decoration for dissimilar values of Ha & Ra when $d_p = 130nm$, $\phi_{hnp} = 0.01$, $\lambda = 0.25$, $\gamma = \frac{\pi}{4}$, $\tau = 0.7$.

Table 3: Variation of average Nu on the heated wall for different γ, Ha and λ when $\phi_{hnp} = 0.01$, $Ra = 10^5$, $d_p = 130nm, \tau = 0.7$.

Ha	γ	Nu_{ave}				
		$\lambda = 0.10$	$\lambda = 0.25$	$\lambda = 0.50$	$\lambda = 0.75$	$\lambda = 1$
5	0	4.6864	5.5708	5.8681	5.9375	5.9632
	$\frac{\pi}{6}$	4.6499	5.6071	5.8834	5.9450	5.9677
	$\frac{\pi}{4}$	4.6414	5.5989	5.8836	5.9455	5.9680
	$\frac{\pi}{3}$	4.8393	5.6882	5.9098	5.9575	5.9749
	$\frac{\pi}{2}$	4.6386	5.6406	5.8974	5.9520	5.9717
45	0	3.4587	3.6341	4.0786	4.4833	4.8054
	$\frac{\pi}{6}$	3.4406	3.5683	3.9494	4.4065	4.7906
	$\frac{\pi}{4}$	3.4273	3.5760	3.9991	4.4198	4.7731

	$\frac{\pi}{3}$	3.4477	3.6341	4.1027	4.5985	4.9730
	$\frac{\pi}{2}$	3.4662	3.5516	3.8929	4.3738	4.7919
100	0	3.4390	3.4667	3.5952	3.7851	3.9893
	$\frac{\pi}{6}$	3.4280	3.4464	3.5394	3.6846	3.8620
	$\frac{\pi}{4}$	3.4162	3.4327	3.5406	3.7159	3.9111
	$\frac{\pi}{3}$	3.4270	3.4568	3.5950	3.7832	3.9998
	$\frac{\pi}{2}$	3.4538	3.4702	3.5314	3.6427	3.8061

diminution with increasing *Ha*, demonstrating a shift from CnV to conduction as the predominant thermal transfer mode.

The CnV within the cavity intensifies due to increasing Rayleigh number values or greater temperature gradients. This results in the isotherms becoming progressively tilted near the colder side walls, while the buoyancy-driven upward movement nearly fills the entire vicinity. Therefore, when the *Ra* is bigger, namely $Ra = 10^6$, the heated fluid from the left side of the cavity flows at a high velocity, resulting in a more efficient transfer of heat to the cold barrier on the right.

Table 4: Average *Nu* (with/without BrM effect) along the heated wall for different values of Ra and ϕ_{hnp}, when $\gamma = \frac{\pi}{4}$, $\lambda = 0.25$, $d_p = 130nm, Ha = 5$, $\tau = 0.7$.

Ra	ϕ_{hnp}	Nu_{ave}			
		With BrM effect	Rise (%)	Without BrM effect	Rise (%)
10^4	0.0	3.2833			
	0.005	3.5247	7.35	3.3789	2.91
	0.01	3.7755	14.99	3.4766	5.89
	0.02	4.3067	31.17	3.6793	12.06
	0.03	4.8775	48.55	3.8918	18.53
10^5	0.0	4.9077			
	0.005	5.2475	6.92	5.0424	2.74
	0.01	5.5989	14.08	5.1798	5.54
	0.02	6.3363	29.11	5.4631	11.31
	0.03	7.1203	45.08	5.7578	17.32
10^6	0.0	8.7351			
	0.005	9.3145	6.63	8.9656	2.64
	0.01	9.9118	13.47	9.2003	5.32
	0.02	11.160	27.76	9.6822	10.84
	0.03	12.480	42.87	10.181	16.55

The table-3, displays the distribution of Nu_{ave} versus λ for different values of γ and Ha along the T_h. It is clear that the Nu_{ave} and HT rate drop as Ha increases. Furthermore, the magnitude of Nu_{ave} rises proportionally with the growing value of λ and is heavily influenced by the γ. Therefore, we can assert that both the γ and λ have a significant impact on the HT analysis. Table-3 shows that the maximum thermal presentation is attained at a specific leaning angle $\gamma = 0$ and $\lambda = 1$.

Table-4, shows the calculated results of Nu_{ave} (with or without BrM effect) along the heated wall for different values of ϕ_{hnp} and Ra, when $\lambda = 0.25$, $Ha = 5, \gamma = \frac{\pi}{4}$, $d_p = 130nm$, $\tau = 0.7$. The input of BrM is showing the NaPs movement inside the cavity which amplified the fluidic temperature. It is evident from the table 4 that the BrM distinguishes a significant role in improvement rate of the temperature distribution. Here a comparison study is performed for the growth of Nu_{ave} for Ra $=10^4 – 10^6$ and ϕ_{hnp} = 0 - 0.03. We found from the tabular results that at $Ra=10^4$ with $\phi_{hnp} = 0.03$, the Nu_{ave} increases 48.55% when the BrM is taken into account, and 18.53% for the other case.

Table 5: Variation of the Nu_{ave} along the heated wall with different mixture ratios of the nanoparticles when $Ra = 10^5$, $\gamma = \frac{\pi}{4}$, $\lambda = 0.25$, $d_p = 130nm, Ha = 5$, $\tau = 0.7$.

ϕ_{Cu}	100%	90%	70%	50%	30%	10%	0%
$\phi_{Al_2O_3}$	0%	10%	30%	50%	70%	90%	100%
Nu_{ave}	5.7090	5.6972	5.6736	5.6498	5.6254	5.5989	5.5813

The average Nu along the cavity's heated wall is shown in Table 5. The influence of hybrid nanoparticle loading and mixing ratios is evaluated using these findings when $Ra=10^5$, $\gamma = \frac{\pi}{4}$, $\lambda = 0.25$, $d_p = 130nm, Ha=5, \tau = 0.7$. According to the findings, *Cu* NaPs in water exhibit the maximum HT rate for the same quantity of NaPs, while Al_2O_3 NaPs in water give the lowest HT rate for a fixed combination ratio. Copper has a higher κ than Al_2O_3, which explains why *Cu* nanoparticles perform better in heat transmission. This behavior has a physical explanation: copper nanoparticles improve the convective heat transfer process by facilitating more effective energy transport. Al_2O_3 has a lower κ than *Cu*, which results in less efficient heat transmission, even if it may improve thermal performance. This illustrates how important it is to choose the right nanoparticles to maximize heat transmission in hybrid nanofluids.

Table 6: For a pure fluid water, the behavior of nanofluid and hybrid NaF for different values of ϕ_{hnp} and Ra, when $\lambda = 0.25, \gamma = \frac{\pi}{4}, d_p = 130nm, Ha = 5, \tau = 0.7$.

Items	ϕ_{hnp}	Nu_{ave}		
		$Ra = 10^4$	$Ra = 10^5$	$Ra = 10^6$
Pure water	0	3.2833	4.9077	8.7351
Al_2O_3-water nanofluid	0.005	3.5198	5.2391	9.2980
	0.01	3.7655	5.5813	9.8776
	0.02	4.2850	6.2985	11.087
	0.03	4.8427	7.0597	12.363

Hybrid nanofluid	0.005	3.5247	5.2475	9.3145
	0.01	3.7755	5.5989	9.9118
	0.02	4.3067	6.3363	11.160
	0.03	4.8775	7.1203	12.480

Table-6 presents the consequence of the average Nusselt number along the left heated barrier for pure H_2O, NaF and hybrid NaF. We estimated the Nu_{ave} along the left heated wall of the vicinity to assess the impact of hybrid nanofluid with a volume percentage of 0.5% - 3% at the Rayleigh number, $Ra = 10^4$-10^6, as presented in Table-6. The table indicates that the rate of thermal transmission escalates with a constant volume percentage of the hybrid nanofluid. The results indicate that the hybrid NaF exhibits the uppermost thermal transmission rate in comparison to pure H_2O and the nanofluid (Al_2O_3-water) across various volume % and Rayleigh number values. The thermal assignment rate markedly upsurges with the same volume % of hybrid nanoparticles in comparison to the Al_2O_3-H_2O NaF. For instance, when the Al_2O_3-H_2O nanofluid is examined, it demonstrates an enhancement of 41.53% at $Ra = 10^6$ with $\phi_{hnp} = 0.03$, while the corresponding increase is 42.87% when the Cu-Al_2O_3/H_2O hybrid nanofluid is investigated. This suggests that the hybrid nanofluid significantly improves heat transfer performance.

4.1. Statistical correlation development

The application of mathematical and statistical methods, particularly ReS methodology, is advantageous for both modeling and scrutinizing problems that involve multiple variables influencing the response of interest. It is widely used in several fields, including as engineering and manufacturing, to enhance and comprehend complex processes. Response surface methodology allows for the assessment of how input variables or factors influence an output response or performance indicator. Researchers may employ mathematical models to analyze the interaction between variables and responses, with the objective of determining the ideal conditions for enhancing heat flow efficiency. This is especially crucial in applications such as heat exchangers and temperature control systems. Investigators can utilize it to simulate and comprehend the complex interrelationships among different components that can be utilized to enhance thermal efficiency in systems that employ nanofluids. The present study demonstrates the influence of the independent variables (λ, d_p and ϕ_{hnp}) on the response function Nu_{ave}, employing the statistical ReS approach. The structure of the quadratic polynomial model is established as follows:

$$y = \beta_0 + \sum_{i=1}^{3} \beta_i x_i + \sum_{i=1}^{3} \beta_{ii} x_i^2 + \sum_{i=1}^{3} \sum_{j=1}^{3} \beta_{ij} x_i x_j \Big|_{i<j} + r \tag{11}$$

The output function, represented by the variable y, is defined by equation (11). The regression coefficient for the linear term of the factor x is represented by the symbol β_i in equation (11), whereas the intercept term is indicated by the symbol β_0. The quadratic term of the i-th and j-th elements is denoted by β_{ij}, while the regression coefficient for the quadratic term of the i-th component is represented by β_{ii}. r is the requested error value. Additionally, it is known that Nu_{ave} is the responsive function (y), and the associated input variables are λ, d_p and ϕ_{hnp}. It is crucial to prioritize the discovery of the response function that most accurately corresponds to the correlation between the independent variables.

Table-7, displays the consequences of the statistical investigation conducted on this model using ReS methodology. The degrees of freedom (DOF) indicate the highest number of independent terms that can be used in this model. The total sum of squares is a statistical measure that quantifies the total amount of variance caused by numerous causes. The mean square has a value of 9.93, which suggests a substantial level of significance. The F-value, which is 42.64 and not due to random variation, demonstrates that the Nu_{ave} model is statistically significant. Furthermore, the p-value is highly significant as an indicator in statistical analysis. The term "accuracy" pertains to the probability that the null hypothesis is true for a certain statistical model. Put simply, a p-value that is extremely low (often ≤ 0.05) indicates that the model is appropriate. Table-6 unambiguously demonstrates that these input features hold substantial importance for our model. Furthermore, the statistical analysis and testing processes of the model reveal a significant R^2 value of 95.16% for Nu_{ave}, which serves as persuasive evidence of the high effectiveness of this model in calculating the response function Nu_{ave}. The ad. R^2 has a value of 92.93%, which is lower than the R^2 score of 95.16% for Nu_{ave}. This framework is relevant for traversing the design space. However, the model still accurately represents the experimental data. Another crucial indicator is the lack-of-fit, which must be minimized to ensure a suitable model. ReS methodology has developed the subsequent generic models for evaluating the

Table 7: ANOVA is utilized to determine Nu_{ave}.

Source	DOF	Sum of Squares	Mean Square	P-value	F-value	Comment
Model	6	59.61	9.93	< 0.0001	42.64	significant
d_p	1	6.77	6.77	0.0001	29.04	
λ	1	6.78	6.78	0.0001	29.12	
ϕ_{hnp}	1	37.41	37.41	< 0.0001	160.54	
$d_p.\lambda$	1	0.1319	0.1319	0.4652	0.5662	
$d_p.\phi_{hnp}$	1	7.94	7.94	< 0.0001	34.07	
$\lambda.\phi_{hnp}$	1	0.5807	0.5807	0.1384	2.49	
Residual error	13	3.03	0.2330			
Pure Error	5	0.0000	0.0000			
Lack of Fit	8	3.03	0.3786			
Core Total	19	62.64				

correlation between the response variable Nu_{ave} and the influential input parameters (λ, d_p and ϕ_{hnp}). The equation can be expressed as:

$$Nu_{ave} = \beta_0 + \beta_1\phi + \beta_2 Ha + \beta_3\lambda + \beta_{11}\phi^2 + \beta_{22}Ha^2 + \beta_{33}\lambda^2 + \beta_{12}\phi Ha + \beta_{13}\phi\lambda + \beta_{23}Ha\lambda \quad (12)$$

The normal distribution is an essential assumption in several statistical analysis and can be established by normality tests. These coefficients are computed based on the input factors λ, d_p, and ϕ_{hnp}. Only the model terms with a p-value of ≤0.05, showing statistical

significance, have been selected to form a valid regression equation because of their significant importance. Conversely, the phrases that lack importance have been ignored. The variables λ, d_p, ϕ_{hnp} and $d_p.\phi_{hnp}$ are significant in the response function Nu_{ave}.

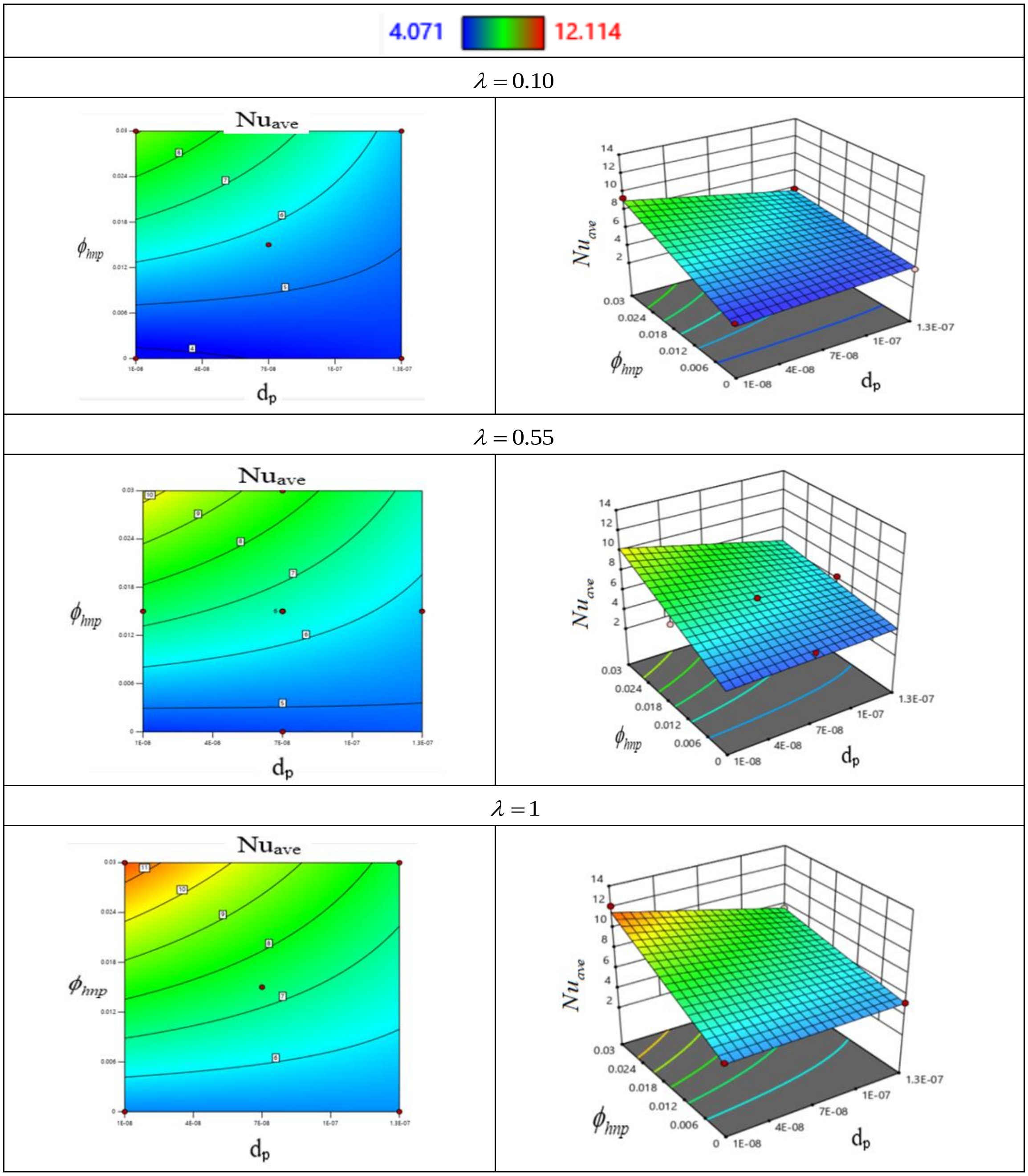

Figure 6: The variations of Nu_{ave} as a function of ϕ_{hnp}, d_p for various values of the λ

The following mathematical correlation summarizes the relationship between the response function Nu_{ave} and the input variables (λ, d_p and ϕ_{hnp}):

$$Nu_{ave} = 6.54 - 0.8226\, d_p + 0.8237\, \lambda + 1.93\, \phi_{hnp} - 0.9961\, d_p.\phi_{hnp} \quad (13)$$

The equation, expressed in coded variables, enables the prediction of the response at designated quantities of each constituent. Each factor is encoded using three levels in the Box-Behnken architecture, with 0 representing the center point and +1 and -1 representing the high and low values that correspond to the cube points, respectively.

4.2. ReS methodology graphical study

A ReS map is a visual depiction that depicts the correlation between multiple independent factors(λ, d_p and ϕ_{hnp}) and the dependent variable Nu_{ave}, derived from computer analysis using response surface. The figure 5 displays two-dimensional and three-dimensional ReS plots derived by ReS methods to analyze the impact of λ, d_p and ϕ_{hnp} on Nu_{ave}. Figure 6 demonstrates that as the value of λ, ϕ_{hnp} increases and d_p declines, the Nu_{ave} value intensifies. The highest value of Nu_{ave} occurs at $\lambda = 1, d_p = 10nm$ and $\phi_{hnp} = 0.03$, while the lowest value is recorded at $\lambda = 0.1, d_p = 130nm$ and $\phi_{hnp} = 0$.

The residual analysis shown in Figures 7(a)–(d) assesses the precision of the RSM methods: The residuals between the anticipated and observed *Nu* (average) are displayed in Figure 7(a), which exhibits a nearly linear trend and indicates that the regression model fits the observed data well. A normal probability map in Figure 7(b) indicates that the residuals are roughly normally distributed. Figure 7(c) displays the internally studentized residuals in comparison to the expected *Nu* (average) values. Indicating that the residual variance is constant across all forecasts, this displays a random scatter without any discernible trend. The model's reliability is further shown by residuals falling within the allowed range of -3 to 3 and a maximum error of about 2.38. The independence of the internally studentized residuals is confirmed in Figure 7(d).

(a)

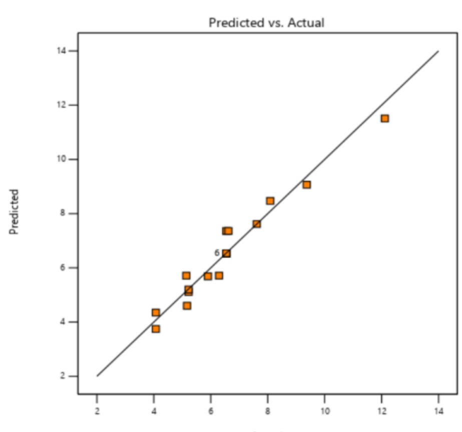

(b)

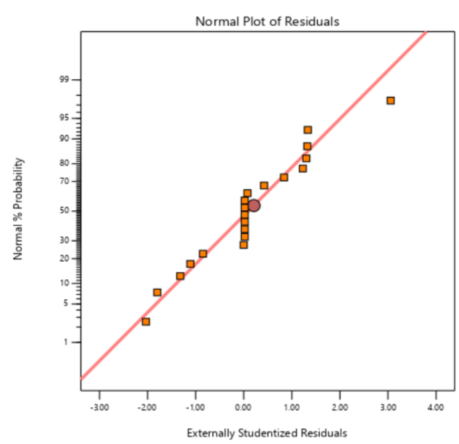

(c)

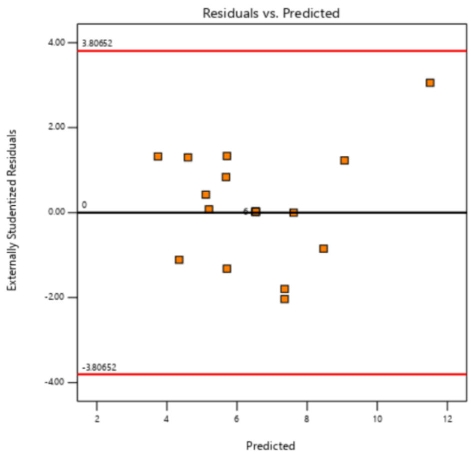

(d)

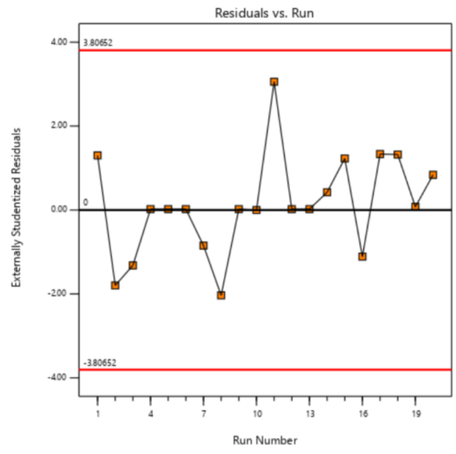

Figure 7: The residual plots include: (a) a plot that contrasts the actual values with the expected values; (b) a normal probability plot of the residual; (c) a plot that compares the studentized residuals to the predicted values; and (d) a plot that compares the internally studentized residual to the run values.

4.3. Sensitivity Analysis

Sensitivity analysis is a crucial technique for studying free convection in hybrid NaFs since it elucidates how vicissitudes in numerous parameters affect the results of the investigation. The rate of heat transfer during the free convective HT of a hybrid NaF can be affected by a number of variables. We can determine the most significant variables and understand how they affect the rate of heat transfer by doing a sensitivity analysis. These tools help to improve the system's performance and optimize its design. Furthermore, sensitivity analysis can help pinpoint the points at which changes in parameters most likely affect the HT rate. The dependent parameter Nu_{ave} partial derivatives with respect to the independent parameters λ, d_p, and ϕ_{hnp} are calculated separately in this work. We effectively obtained the desired outcomes by adjusting the independent variable values at three different levels (low, moderate, and high), denoted by the numbers -1, 0, and 1, respectively. The sensitivity is determined using the regression Equation (13) as a guide. The partial derivative of the output function Nu_{ave} with respect to the independent components is calculated in order to quantify sensitivity (Keya et al. 2024). The following are the response function's subsequent sensitivity functions:

$$\frac{\partial Nu_{ave}}{\partial \lambda} = 0.8237 \tag{14}$$

$$\frac{\partial Nu_{ave}}{\partial d_p} = -0.8226 - 0.9961\phi_{hnp} \tag{15}$$

$$\frac{\partial Nu_{ave}}{\partial \phi_{hnp}} = 1.93 - 0.9961 d_p \tag{16}$$

The output function value is directly enhanced by an increase in the input variable value, as indicated by a positive sensitivity output. Additionally, a negative sensitivity value suggests that an increase in the input variable leads to a decrease in the output function. Figure 8 and Table-8 illustrate the sensitivity analysis of the Nu_{ave} output response for a variety of λ, d_p and ϕ_{hnp} values. The data indicates that the sensitivity of λ and ϕ_{hnp} is positively correlated, whereas the sensitivity of d_p is negatively correlated. Consequently, the relationship between d_p and Nu_{ave} is inverse, indicating that a rise in d_p leads to a decrease in Nu_{ave}. In contrast, the Nu_{ave} is positively affected by the variables λ and ϕ_{hnp}. This is as a result of their direct impact on thermal transfer and fluid flow. The HT rate can be improved by increasing these parameters. Nu_{ave} exhibits the highest degree of sensitivity to ϕ_{hnp} among these parameters.

Table 8: Sensitivity study of Nu_{ave}

ϕ_{hnp}	λ	d_p	$\frac{\partial Nu_{ave}}{\partial d_p}$	$\frac{\partial Nu_{ave}}{\partial \lambda}$	$\frac{\partial Nu_{ave}}{\partial \phi_{hnp}}$
0	-1	-1	-0.8226	0.8237	2.9261
		0	-0.8226	0.8237	1.93
		1	-0.8226	0.8237	0.9339
	0	-1	-0.8226	0.8237	2.9261
		0	-0.8226	0.8237	1.93
		1	-0.8226	0.8237	0.9339
	1	-1	-0.8226	0.8237	2.9261
		0	-0.8226	0.8237	1.93
		1	-0.8226	0.8237	0.9339

(a)

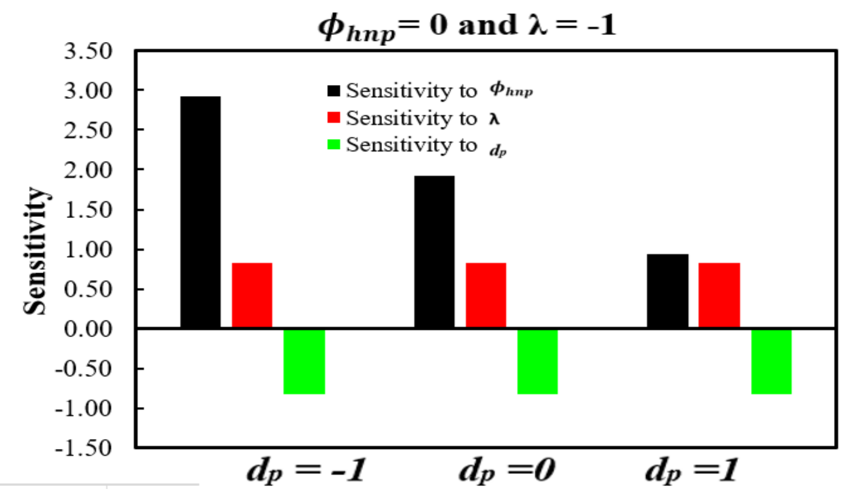

(b)

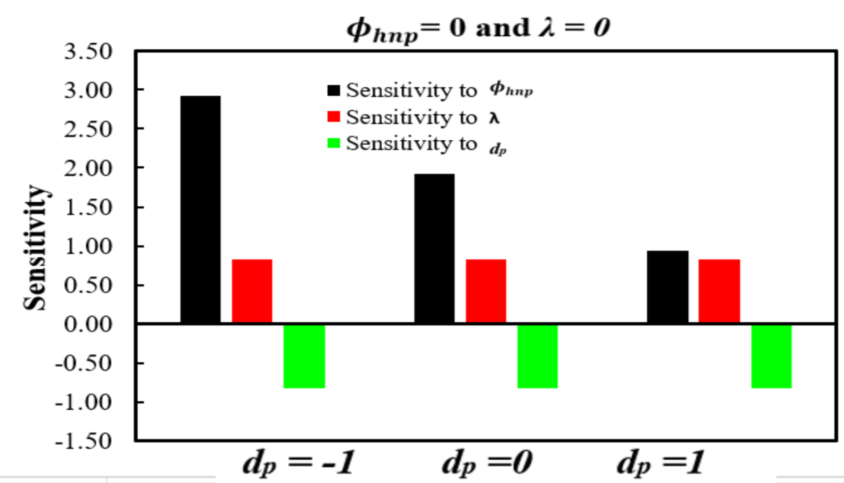

(c)

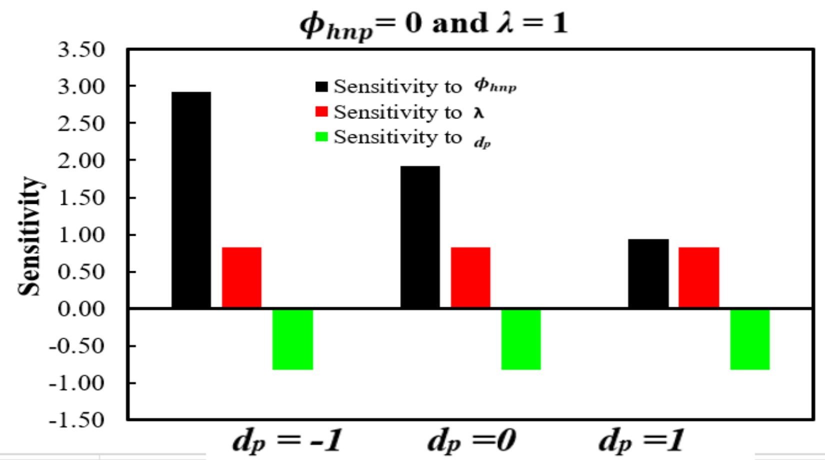

Figure 8: Sensitivity analysis results of Nu_{ave} for different coded levels of d_p (low, medium, high) (a) at $\phi_{hnp} = 0$ and λ = -1 (b) $\phi_{hnp} = 0$ and λ = 0 (c) $\phi_{hnp} = 0$ and λ = 1.

4.4. Optimization analysis

Response surface methodology can be utilized to determine the minimum and maximum values of one or several replies. To ascertain the optimal conditions for diverse reactions, such as product yield and growth, one may analyze the contour plot of the ReS generated by the regression models. This graphical optimization technique enables the precise identification of the specific region inside the parameter space where the desired response can be attained and assists in locating the area that fulfills the optimal requirements. The optimization study of an experimental design is assessed by three distinct methodologies: point prediction, graphical analysis, and numerical analysis. In numerical optimization, the selection of answers and factors is contingent upon the specific purpose of the investigation. The responses are generated in 3 distinct formats: ramps, bar graphs and report graphs, all addressing the same issue.

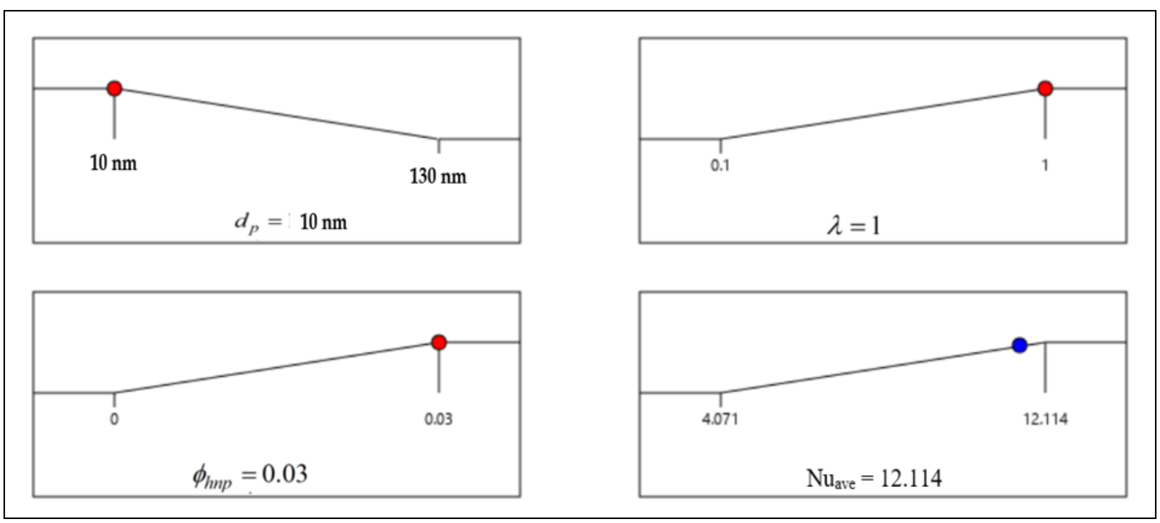

Figure 9: Statistically optimize for a ramp chart for Nu_{ave}

Investigators frequently utilize ramps as a visual representation of the optimization outcomes, as seen in Figure 9. This illustration exemplifies the concept of numerical optimization. The implications suggest that the ideal value of Nu_{ave} is 12.114, which is obtained when $\lambda = 1, d_p = 10nm$ and $\phi_{hnp} = 0.03$. The optimal values are obtained for 3 relevant parameters (λ, d_p and ϕ_{hnp}). By putting these values in equation (13), the Nu_{ave} can be calculated, and the best optimal point is obtained.

The present framework's model limitations include the potential oversimplification of complex phenomena due to the reliance on single-phase model assumptions and the neglect of radiation effects. For example, in high-energy environments or under extreme conditions, the absence of radiation can lead to inaccurate temperature predictions and thermal behavior. In the same vein, the applicability of single-phase models to real-world scenarios may be restricted by their inability to accurately represent the interactions between various phases in multiphase systems. In order to overcome these constraints in forthcoming investigations, researchers could integrate radiation transport equations and create multiphase models that incorporate the interactions between phases, thereby enhancing the model's predictive capabilities and fidelity. Furthermore, the models' robustness and accuracy could be further improved by integrating advanced computational techniques, such as computational fluid dynamics and machine learning methods, and experimental validation.

5. Conclusions

This study aims to analyze the optimization of unsteady free convection HT of $Cu\text{-}Al_2O_3/H_2O$ hybrid NaF within a square cavity under an oblique periodic magnetic field using the finite element method coupled with response surface methodology. The graphical and tabular representations depict the effects of certain constraints (*Ha, Ra,* λ, ϒ, ϕ_{hnp},d_p and Nu_{ave}). The deductions presented are derived from the current numerical computations. The overall HT rate decreases as the values of d_p and *Ha* grow. The HT rate increases as the values of λ, Ra and ϕ_{hnp} rise. The maximum rate of thermal transmission is attained at $\gamma = \pi/2$ when $\lambda = 1$. When the BrM of the nanoparticles is engaged into consideration of the ThC model, the thermal transmission rate increases by 48.55% at $Ra = 10^4$ with $\phi_{hnp} = 0.03$, however the increase is only 18.53% in the circumstance where the BrM is not considered. The hybrid NaF may exhibit the uppermost HT rate in comparison to pure H_2O and the mono NaF. For instance, when the $Al_2O_3\text{-}H_2O$ nanofluid is examined, it demonstrates an enhancement of 41.53% at $Ra = 10^6$ with $\phi_{hnp} = 0.03$, while the corresponding increase is 42.87% when the $Cu\text{-}Al_2O_3/H_2O$ hybrid nanofluid is investigated that is the incorporation of hybrid nanoparticles enhances the rate of thermal transfer. The HT in the $Cu\text{-}Al_2O_3$/water hybrid NaF upsurges as the *Cu* NaP ratio rises at a specific volume fraction. In contrast, the ratio of Al_2O_3 nanoparticles decreases, which leads to a decrease in HT. A correlation eqn. has been formulated using the ReS policy to ascertain the relationship between the output response and input variables. This equation facilitates the attainment of the optimal value for mean *Nu*, hence maximizing the rate of heat transmission. The ideal condition was identified at $\lambda = 1, d_p = 10nm$ and $\phi_{hnp} = 0.03$, and the resulting Nu_{ave} value was calculated to be 12.114. The rate of heat transmission is positively sensitive to variations in λ and the volume percentage of hybrid nanoparticles and hybrid nanoparticles exhibit negative sensitivity to their diameters toward thermal transport rates.

This finding makes it clear what more study needs to be done and how it can be used in the real world in the areas of HT and fluid dynamics. It is very important to look into this study further because it could be useful in many areas. The present study can be widened to include porous media by using machine learning.

Nomenclature			
Symbols	**Descriptions**	hnp	Hybrid nanoparticles
c_p	Specific heat *[$Jkg^{-1}K^{-1}$]*	hnf	Hybrid NaF
B_0	MaF strength [$Nm^{-1}A^{-1}$]	NPs	Nanoparticles
d_p	Diameter of hybrid NPs [nm]	ave	Average
D_T^l	Numeric value of D_T	a	Al_2O_3
D_T	Thermal diffusion coefficient $[\mathrm{m^2s^{-1}}]$	c	Cu
Ra	Rayleigh number	**Greek symbols**	
$\boldsymbol{g}$	Gravitational acceleration [ms^{-2}]	μ	Dynamic viscosity [Nsm^{-2}]
Ha	Hartmann number	θ	Dimensionless temperature
L	Cavity length[m]	σ	Electric conductivity [s/m]
p	Fluid pressure [Pa]	υ	Kinematic viscosity [m^2s^{-l}]
k_B	Boltzmann constant $[\mathrm{JK^{-1}}]$	ϕ	Volume fraction
t	Dimensional time[s]	λ_0	Period
X,Y	Dimensionless coordinates	ρ	Density [kgm^{-3}]
Pr	Prandtl number	κ	Thermal conductivity [$Wm^{-1}K^{-1}$]
u,v	Velocity components in x ,y directions[ms^{-l}]	α	Thermal diffusivity [m^2s^{-l}]
x,y	Cartesian coordinates *[m]*	γ	Magnetic field inclination angle [rad]
T_{ref}	Reference temperature	β	Thermal expansion coefficient [$1/K$]
Nu	Nusselt number	τ	Dimensionless time
U,V	Dimensionless velocity components	**Abbreviations**	
T	Fluid Temperature [K]	BC	Boundary condition
Subscripts		VF	Volume fraction
bf	Base fluid	ReS	Response surface
c_1	Cold	FEM	Finite element method
h	Hot	TpC	Thermophysical correlation

Acknowledgements

We are grateful to the anonymous reviewers for their constructive comments and suggestions for the further improvement of the paper.

References

Alam MS, Huda MN, Rahman MM, Billah MM.2024. Statistical and numerical analysis of magnetic field effects on laminar natural convection heat transfer of nanofluid in a hexagonal cavity. Int. J. Thermofluids, 24: 100856, 2024. https://doi.org/10.1016/j.ijft.2024.100856

Alam MS, Huda MN, Hossain SMC. 2023. Hydromagnetic convective heat transfer in a square cavity filled with Fe_3O_4-water nanofluid saturated porous medium, Jagannath University Journal of Science 10 (II): 145-158.

Alam S, Rahman M, Parvin S, Vajravelu K. 2016. Finite Element Simulation for Heatline Visualization of Natural Convective Flow and Heat Transfer inside a Prismatic Enclosure, Int. J. Heat and Technology, 34: 391-400.

Ben-Cheikh N, Chamkha AJ, Ben-Beya B, Lili T. 2013. Natural convection of water based nanofluids in a square enclosure with non-uniform heating of the bottom wall, J. Modern Phys. 04(02): 147-159.

Belhaj S, Ben-Beya B. 2022. Thermal performance analysis of hybrid nanofluid natural convection in a square cavity containing an elliptical obstacle under variable magnetic field, Int. J. Numerical Methods for Heat & Fluid Flow, 32(6): 1825-1860.

Choi SUS. 1995. Enhancing thermal conductivity of fluids with nanoparticles, In. Proceedings of the 1995 ASME Int. Mechanical Engineering Congress and Exposition, San Francisco, USA. ASME, FED 231/MD,66: 99-105.

De Vahl Davis G. 1983. Natural convection of air in a square cavity: A bench mark numerical solution, Int. J. Numerical Methods in Fluids, 3(3): 249-264.

Devi SU, Devi SA. 2017. Heat transfer enhancement of $Cu\text{-}Al_2O_3$/water hybrid nanofluid flow over a stretching sheet, J. Nigerian Mathematical Society, 36(2): 419-433.

Ghasemi B, Aminossadati SM, Raisi A. 2011. Magnetic field effect on natural convection in a nanofluid-filled square enclosure. Int. J. Thermal Sciences, 50: 1748-1756.

Haque MM, Alam MS, Huda MN, Rahman MM.2024. Statistical and Numerical Investigations of Convective Heat $Al_2O_3\text{-}Cu$/water Transfer Enhancement of Nanofluids Inside a Rectotrapezoidal Enclosure in the Presence of Horizontal Periodic Magnetic Field. Arabian Journal for Science and Engineering, https:// doi.org/10.1007/s13369-024-09596-0

Ho CJ, Liu WK, Chang YS, Lin CC. 2010. Natural convection heat transfer of alumina-water nanofluid in vertical square enclosure: an experimental study, Int. J. Thermal Sciences,49: 1345-1353.

Jana S, Salehi-Khojin A, Zhong WH. 2007. Enhancement of fluid thermal conductivity by the addition of single and hybrid nano-additives, Thermochimica Acta, 462(1-2): 45-55.

Keya SS, Alam MS, Huda MN, Rahman MM.2024. Optimization and sensitivity analysis of natural convective heat transfer of nanofluids inside a quarter-circular enclosure using response surface methodology,J. Fluid Flow, Heat and Mass Transfer, 11: 220-232.

Maxwell JC. 1873. Electricity and magnetism, Clarendon Press, Oxford, UK.

Rahman MM, Saghir Z, Pop I. 2022. Free convective heat transfer efficiency inhybrid nanofluid inside a rectotrapezoidal enclosure, Int. J. Numer. Meth. Heat & Fluid Flow, 32(1): 196-218.

Suresh S, Venkitaraj KP, Selvakumar P, Chandrasekar M. 2011. Synthesis of Al_2O_3-Cu/Water hybrid nanofluids using two step method and its thermo physical properties, Colloids and Surfaces, A Physicochemical and Engineering Aspects, 388(1-3): 41- 48.

Sivaraj C, Sheremet MA. 2017. MHD natural convection in an inclined square porous cavity with a heat conducting solid block, J. Magn. Magn. Mater. 426: 351-360.

Yildiz C, Arici M, Karabay H. 2019. Comparison of a theoretical and experimental thermal conductivity model on the heat transfer performance of Al_2O_3-SiO_2/water hybrid nanofluid, Int. J. Heat. Mass Transf. 140: 598-605.

Zienkiewicz OC, Taylor RL. 1991. The finite element method, 4th Edition, McGraw-Hill.